Environmental Science Nano

ROYAL SOCIETY OF CHEMISTRY

COMMUNICATION

View Article Online
View Journal | View Issue

Cite this: *Environ. Sci.: Nano*, 2026, **13**, 2262

Received 28th February 2026,
Accepted 17th April 2026

DOI: 10.1039/d6en00180g

rsc.li/es-nano

Visualizing hydrogen nanobubble generation at nanoscale zero-valent iron/water interfaces

Shuangjia Shi,[a] Qing Huang,*[abc] Wei-xian Zhang,[a] Lijuan Zhang*[bde] and Airong Liu *[a]

Nanobubbles (NBs) possess unique interfacial and physicochemical properties, yet convincing in-liquid, nanoscale-resolved evidence of their formation in reactive metal–water systems remains lacking. Here, we visualize hydrogen nanobubble (HNB) generation during the anaerobic aqueous corrosion of nanoscale zero-valent iron (nZVI) using optical scattering methods, synchrotron imaging and interfacial microscopy. Laser Tyndall scattering and nanoparticle tracking analyses reveal fast-moving nanoscale scattering centers in 0.22 μm filtered nZVI–H_2O reaction filtrates; these signals are negligible in ethanol controls and are strongly suppressed by freeze–vacuum degassing, supporting a gaseous origin. In-liquid scanning transmission X-ray microscopy at the O K-edge resolves discrete high-transmission void-like features adjacent to nZVI aggregates in water but not in ethanol, directly visualizing interfacial gas domains. Liquid-phase scanning electron microscopy and atomic force microscopy show that these low-density, low-stiffness domains emerge rapidly and accumulate at the iron/water interface. Cyclic voltammetry and electron paramagnetic resonance spin trapping further link gas-domain formation to sustained hydrogen evolution and short-lived hydrogen-associated intermediates. These results establish aqueous nZVI corrosion as an intrinsic generator of HNBs and extend iron corrosion from a classical solid–liquid pathway to coupled gas–liquid–solid interfacial processes, which have implications for groundwater remediation.

Environmental significance

Nanoscale zero-valent iron (nZVI) is widely used in groundwater remediation, yet its corrosion is typically viewed as a solid–liquid redox process. Whether corrosion-generated hydrogen remains dissolved or forms interfacial gas phases has remained unclear. Here, we show that aqueous nZVI corrosion intrinsically produces hydrogen nanobubbles at the iron/water interface. Using light scattering, nanoparticle tracking analysis, scanning transmission X-ray microscopy, liquid-phase microscopies, and electrochemical/spin-spectroscopic tools, we directly visualize these nanoscale gas domains and link them to sustained hydrogen evolution. This work reframes iron corrosion as a coupled gas–liquid–solid process relevant to remediation performance.

Introduction

Nanobubbles (NBs) are gas-filled cavities smaller than 1 micrometer (μm) that exhibit unusual stability and interfacial reactivity in water,[1–3] underpinning a wide range of applications in advanced oxidation, flotation, catalysis, and biomedical treatment.[4–9] Despite extensive technological efforts to generate NBs through hydrodynamic cavitation, electrolysis, membrane dispersion, and ultrasonication,[10–12] the possibility that reactive nanomaterials themselves could act as intrinsic, reaction-driven NB sources remains largely unexplored. Nanoscale zero-valent iron (nZVI), a widely employed nanomaterial in environmental remediation,[13–15] offers a compelling case. Under anaerobic aqueous conditions, nZVI undergoes corrosion with water to release hydrogen (H_2, eqn (1)). Although this reaction is thermodynamically unfavorable under standard conditions, it can proceed in natural systems because the low activities of Fe^{2+}, OH^-, and H_2 shift the Gibbs free energy toward interfacial H_2 generation.[16,17] However, a critical question remains unresolved: does the H_2 generated during nZVI corrosion remain dissolved, or does it nucleate into hydrogen nanobubbles (HNBs)?

$$Fe + 2H_2O = Fe^{2+} + H_2 + 2OH^- \quad (1)$$

The corrosion-induced H_2 evolution rate of nZVI can reach approximately 4.9 g H_2 kg^{-1} Fe h^{-1} (corresponding to ~4.9 mg H_2 L^{-1} h^{-1} at an nZVI loading of 1 g L^{-1}),[18] which exceeds the solubility of H_2 predicted by Henry's law (≈1.6 mg L^{-1} at

[a] *State Key Laboratory of Water Pollution Control and Green Resource Recycling, College of Environmental Science and Engineering, Tongji University, Shanghai 200092, China. E-mail: liuairong@tongji.edu.cn*
[b] *Shanghai Synchrotron Radiation Facility, Shanghai Advanced Research Institute, Chinese Academy of Sciences, Shanghai 201204, China. E-mail: zhanglijuan@sari.ac.cn*
[c] *Faculty of Chemical Engineering and Energy Technology, Shanghai Institute of Technology, Shanghai 201418, China. E-mail: hq@sit.edu.cn*
[d] *University of the Chinese Academy of Sciences, Beijing 100049, China*
[e] *Shanghai Institute of Applied Physics, Chinese Academy of Sciences, Shanghai 201800, China*

20 °C and 1 atm). This continuous generation readily drives local supersaturation at the iron/water interface, where nanoscale roughness and corrosion pits provide favorable sites for heterogeneous nucleation.[19,20] These considerations suggest that aqueous nZVI corrosion could intrinsically produce HNBs. However, prior studies have focused primarily on the contaminant transformation pathways or hydrogen generation,[21,22] leaving the existence and interfacial evolution of HNBs in this system essentially unknown. Although HNBs integrate the reductive and antioxidative functionalities of molecular hydrogen with the exceptional interfacial reactivity and long-term stability characteristic of nanobubbles,[23–27] their behavior in reactive metal–water systems remains poorly understood. Their nanoscale size, optical transparency, and rapid evolution further hinder in-liquid visualization, and direct nanoscale-resolved evidence of their interfacial formation remains lacking.

Establishing the existence of such nanoscale gas domains requires complementary approaches that can detect nanoscale features in suspension, directly visualize interfacial gas domains, and link these observations to hydrogen-evolving corrosion chemistry. No single technique can resolve all of these aspects. Accordingly, we combine light scattering and nanoparticle tracking analysis (NTA) for suspension-scale detection, scanning transmission X-ray microscopy (STXM) for direct interfacial visualization, liquid-phase scanning electron microscopy (L-SEM) and atomic force microscopy (AFM) for tracking interfacial evolution, and cyclic voltammetry (CV)/electron paramagnetic resonance (EPR) for probing the underlying hydrogen-evolving surface chemistry. This integrated framework enables direct visualization of HNB formation at the iron/water interface and captures their evolution across multiple spatial and temporal scales.

Together, these complementary tools allow us to: (1) confirm the intrinsic generation of HNBs during aqueous nZVI corrosion; (2) reveal their evolving interfacial morphology and dispersion; and (3) provide direct nanoscale-resolved evidence of gas-domain formation in a reactive metal–water system, advancing the mechanistic understanding of HNB formation and informing greener strategies for groundwater remediation.

Materials and methods

Chemicals and materials

All reagents were of analytical grade and were used without further purification. Complete information on chemical sources is provided in Text S1. nZVI was synthesized *via* the liquid-phase reduction of $FeCl_3{\cdot}6H_2O$ with $NaBH_4$, as reported previously.[28,29] Detailed procedures are provided in Text S2. Unless otherwise noted, all experiments were performed under anaerobic conditions, with dissolved oxygen reduced to ~0 mg L^{-1} after 10 min of N_2 purging (Fig. S4). Deionized water (18.2 MΩ cm) was used for solution preparation.

Visualization and characterization of HNBs

To investigate the formation of HNBs during aqueous nZVI corrosion across complementary length and temporal scales, we combined optical scattering and nanoparticle tracking with in-liquid microscopies and electrochemical/spectroscopic assays. Tyndall scattering and NTA were performed on 0.22 μm-filtered reaction filtrates. Synchrotron-based STXM was conducted at the O K-edge to distinguish water from low-density gas domains. The AFM PeakForce quantitative nanomechanical mode and L-SEM were used to capture early-stage interfacial evolution during aqueous corrosion. Detailed workflows and instrument configurations are provided in the SI (Text S3–S6).

Detection of reactive species

Electrochemical hydrogen evolution was assessed *via* cyclic voltammetry in N_2-saturated 50 mM Na_2SO_4 electrolyte, and reactive intermediates were detected *via* EPR spectroscopy using DMPO spin trapping. Detailed experimental procedures are provided in the SI (Text S7 and S8).

Results and discussion

Light-based evidence for nanobubble entities in suspension

Laser illumination of the 0.22 μm-filtered suspensions revealed a clear, medium-dependent Tyndall scattering response (Fig. 1a–c). Under identical optical settings, the filtrate from the nZVI–H_2O system produced a distinct Tyndall path, whereas the nZVI–ethanol control and the degassed H_2O sample showed no visible scattering, indicating that nanoscale scattering centers emerge specifically under aqueous corrosion conditions.

NTA further confirmed the presence of abundant, rapidly moving scattering centers in the nZVI–H_2O filtrates across nZVI loadings (0–400 mg L^{-1}) (Fig. 1i–m), while signals remained negligible in the nZVI–ethanol filtrates (Fig. 1d–h) and were largely suppressed after freeze–vacuum degassing (Fig. 1n–r). Because 0.22 μm filtration removes most iron particulate aggregates (TEM control in Fig. S5), and because the remaining entities exhibit fast trajectories in Video S1, the observed NTA signals are more consistent with nanoscale gas domains rather than residual nZVI particles. Collectively, the optical and NTA data establish that aqueous nZVI corrosion generates a population of dispersible nanoscale entities that is absent in the ethanol control and strongly diminished by degassing, consistent with nanobubbles.

Quantitative NTA analysis (Fig. S6, reproduced from our group's previous work[30]) further showed that the number density of nanoscale entities in the nZVI–H_2O system increases progressively with both reaction time (0–120 min) and nZVI loading (20–200 mg L^{-1}, after 0.22 μm filtration). The dependence on nZVI loading is monotonic but not strictly linear, with a more pronounced increase at higher loadings (>100 mg L^{-1}). This suggests that hydrogen generation and the resulting nanobubble population increase

Fig. 1 Light-based signatures of nanoscale gas domains generated during aqueous nZVI corrosion. (a–c) Representative photographs showing Tyndall scattering under identical laser illumination for 0.22 μm-filtered suspensions containing nZVI (100 mg L^{-1}) in C_2H_5OH (a), deionized water (DIW) (b), and DIW after freeze–vacuum degassing (c). (d–r) Representative NTA camera frames of filtrates from nZVI–C_2H_5OH (d–h), nZVI–H_2O (i–m), and degassed nZVI–H_2O (n–r) at nZVI loadings of 0, 50, 100, 200 and 400 mg L^{-1}. Conditions: unless stated otherwise, suspensions were reacted for 120 min prior to 0.22 μm filtration and NTA measurement; degassing was performed by freeze–vacuum treatment.

nonlinearly with the amount of reactive iron present. Importantly, freeze–vacuum degassing markedly suppresses the measured number densities across conditions, providing further support for the entities detected *via* NTA originating predominantly from hydrogen nanobubbles generated during the nZVI–H_2O reaction. These suspension-scale observations motivated us to conduct direct interfacial imaging to determine whether these dispersible entities originated from gas domains formed at the reactive nZVI/water interface.

Synchrotron STXM visualization of interfacial gas domains

To directly test whether the aqueous scattering entities corresponded to interfacial gas domains, we performed in-liquid STXM at the O K-edge (540 eV), at which strong absorption by water yields high contrast against low-density voids. Both the ethanol and aqueous suspensions formed stable thin liquid layers suitable for soft X-ray transmission, as verified by the presence of continuous optical interference rings before imaging (Fig. 2a and b). In the nZVI–C_2H_5OH system, the contrast remained confined to the particulate aggregates and their immediate vicinity, and no discrete circular high-transmission features were detected (Fig. 2c). Conversely, the nZVI–H_2O system exhibited numerous circular high-transmission features adjacent to, and occasionally within, nZVI aggregates (Fig. 2d), consistent with low-density nanoscale gas pockets in water. The preferential occurrence of these domains at/near aggregates is consistent with reaction-driven gas formation, because aggregates provide confined microenvironments and heterogeneous nucleation sites that favor local H_2 supersaturation and gas-domain formation.

Notably, the gas domains coincide with a more open, porous ("hollow-like") aggregate morphology compared to that of the ethanol control. This observation provides support for a bubble-assisted restructuring scenario in which interparticle gas pockets act as transient spacers. Once nucleated, nanoscopic gas domains can occupy inter-aggregate voids, locally displace liquid, and mechanically separate adjacent primary particles to produce the hollow-like interparticle microstructures resolved *via* STXM. This is consistent with a recent report that interfacial nanobubbles can direct local structure formation during interfacial processes.[31] These interfacial gas pockets are also expected to alter mass transfer by creating localized gas–liquid interfaces and shortening diffusion lengths for dissolved H_2 near reactive sites, thereby coupling corrosion kinetics and interfacial structure. Overall, STXM provides nanoscale, in-liquid evidence that the hydrogen generated during aqueous nZVI corrosion does not solely remain dissolved, but partitions into discrete interfacial gas domains. This interfacial picture helps to explain the dispersible entities detected *via* NTA and is further supported by the time-dependent interfacial evolution observed *via* L-SEM and AFM.

Interfacial imaging by L-SEM and AFM reveals time-dependent gas-domain evolution

Time-resolved interfacial imaging revealed the rapid emergence and growth of low-density domains during aqueous nZVI corrosion. In L-SEM, the nZVI–C_2H_5OH control showed stable aggregates over 0–2 min without

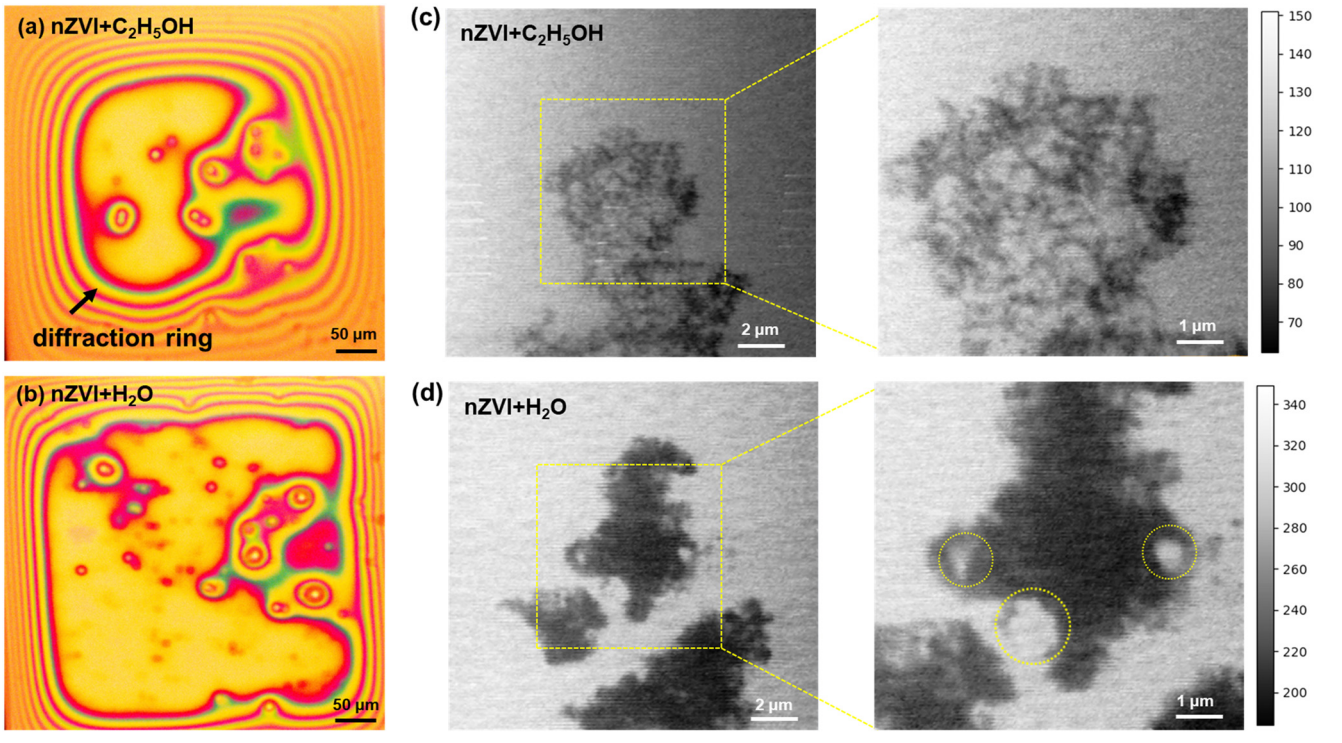

Fig. 2 STXM resolves interfacial gas domains in the aqueous nZVI system. (a) Optical micrograph of the sealed liquid layer for nZVI–C_2H_5OH, showing interference rings indicative of a suitable film thickness for soft X-ray transmission. (b) Optical micrograph of the sealed liquid layer for nZVI–H_2O (DIW), showing comparable interference rings. (c) In-liquid STXM image of nZVI–C_2H_5OH at the O K-edge (540 eV), showing uniform contrast around nZVI aggregates. (d) In-liquid STXM image of nZVI–H_2O (DIW), revealing circular high-transmission regions adjacent to nZVI aggregates (dashed circles in inset), consistent with low-density gas domains. Scale bars: 50 μm (a and b); 2 μm (c and d, left); 1 μm (c and d, inset).

circular low-contrast features (Fig. 3a). In contrast, in the nZVI–H_2O system, circular low-contrast spots appeared adjacent to aggregates within ~1 min and evolved into a more diffuse low-density interfacial gas region by ~2 min (Fig. 3b), indicating water-specific interfacial restructuring during corrosion.[32] The same pattern was reproduced across multiple locations, providing support for the features being intrinsic to the aqueous reaction rather than beam-induced artefacts.

AFM further corroborated these domains through mechanical-contrast imaging. Upon introducing deionized water to surface-deposited nZVI, the discrete circular

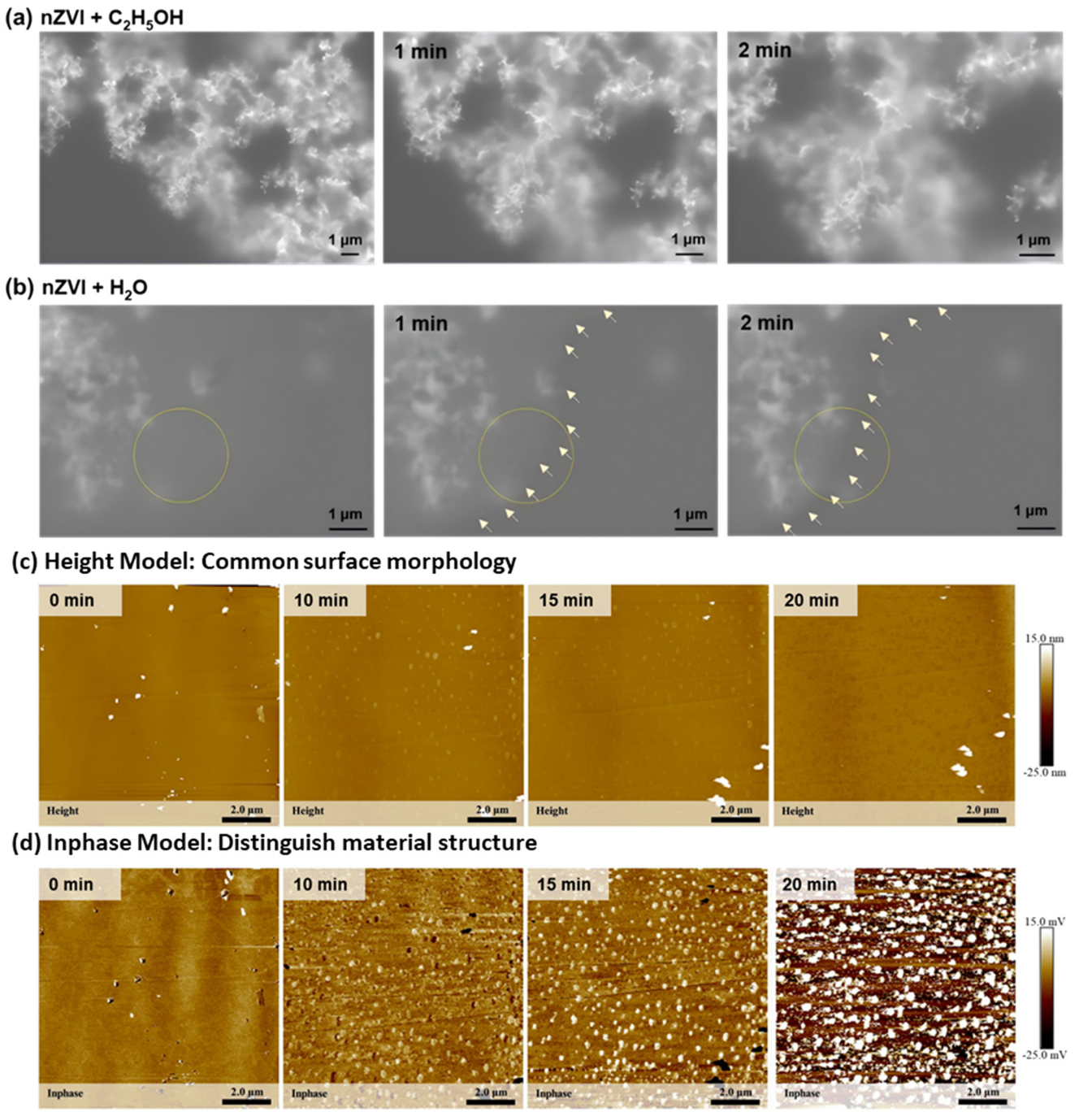

Fig. 3 Time-resolved L-SEM and AFM resolve early-stage interfacial gas-domain evolution during aqueous nZVI corrosion. (a) L-SEM snapshots of nZVI–C_2H_5OH (0–2 min), showing stable aggregates without circular low-contrast domains. (b) L-SEM snapshots of nZVI–H_2O (DIW) (0–2 min), in which circular low-contrast domains emerge within ~1 min and develop into a diffuse low-density interfacial gas region by ~2 min (circle/arrows). (c) AFM height maps (0–20 min) capturing the surface morphology after introducing degassed DIW. (d) AFM in-phase maps (0–20 min) selectively resolving low-stiffness domains that increase over time. Scale bars: 1 μm (a and b); 2 μm (c and d).

features increased progressively and became prominent within ~10 min, with substantially higher abundance by ~20 min (Fig. 3c and d). Height maps primarily report morphology and cannot always separate nascent domains from particle topography; in contrast, in-phase contrast selectively highlights mechanically compliant regions distinct from the stiff nZVI solids. The combined L-SEM and AFM observations therefore support the time-dependent accumulation of soft, low-density interfacial entities during nZVI–H_2O corrosion, consistent with the formation and evolution of nanoscopic gas domains.

Taken together with the light-scattering/NTA and STXM results, these observations support a unified picture in which hydrogen nanobubbles nucleate within confined reactive interfacial microenvironments, where local reactant enrichment and interfacial confinement may favor gas-domain formation, and persist or are continuously replenished during ongoing corrosion.[19,33,34] While coalescence into larger bubbles cannot be excluded, the present observations are more consistent with a dynamic interfacial steady state dominated by nanoscale gas domains. In our previous studies,[30,35] HNB-containing nZVI systems showed enhanced reductive removal of groundwater contaminants, including Se(IV) and As(III), indicating that HNB-associated interfacial processes may contribute to contaminant reduction in nZVI-based remediation, consistent with a recent report on iron-based nanomaterials for water purification.[36]

Electrochemical and EPR spin-trapping evidence for hydrogen species associated with nanobubble formation

To connect interfacial gas-domain formation with the underlying hydrogen-evolving surface chemistry, we interrogated corrosion-driven hydrogen pathways using CV and EPR spin trapping (Fig. 4). In aqueous media, nZVI corrosion proceeds through coupled anodic iron oxidation and cathodic water reduction at the heterogeneous Fe^0/oxide interface. The CV response of the nZVI–H_2O system displays a dominant hydrogen-evolution feature, along with a weaker contribution from adsorbed hydrogen intermediates (H*). This indicates continuous interfacial water reduction, with surface-bound hydrogen forming transiently *en route* to H_2 (Fig. 4a). This behavior is consistent with localized H_2 generation at discrete reactive micro-sites, providing a chemical basis for the interfacial gas domains inferred from imaging.

EPR provides complementary evidence that interfacial chemistry involving hydrogen is uniquely activated during aqueous corrosion. Spin-trapped radical signals are observed only in the nZVI–H_2O system, whereas the ethanol control and water blank remain featureless[37,38] (Fig. 4b), indicating that short-lived hydrogen-associated intermediates arise specifically from nZVI–H_2O interfacial reactions. Quantitative spin analysis further shows that the accumulated spin concentration increases progressively with reaction time, from 0.1794×10^{15}

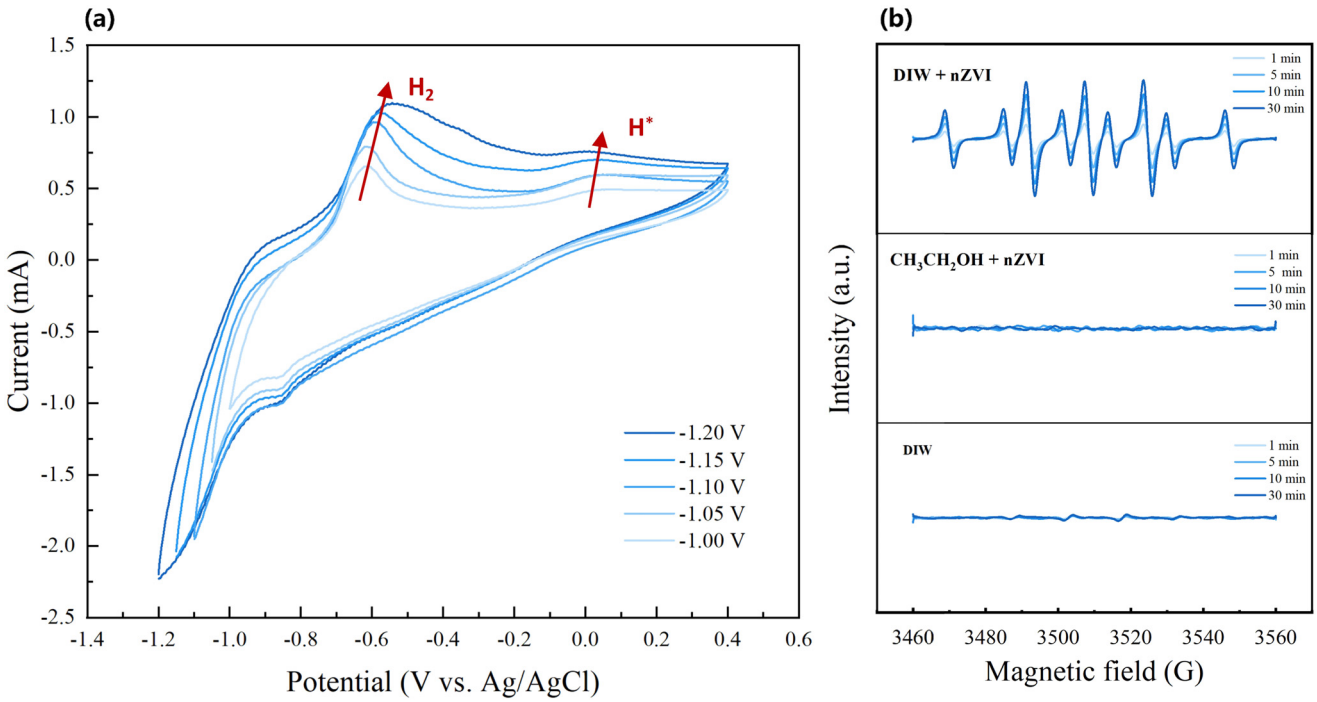

Fig. 4 Electrochemical and EPR identification of hydrogen species associated with nanobubble formation during aqueous nZVI corrosion. (a) Cyclic voltammograms of the nZVI–H_2O (anaerobic DIW) system showing a dominant hydrogen-evolution feature and a weaker contribution attributed to adsorbed hydrogen intermediates (H*). (b) Time-resolved EPR spectra (DMPO spin trapping) collected from the nZVI–H_2O system, with nZVI–C_2H_5OH and H_2O controls shown for comparison. Conditions: nZVI = 100 mg L^{-1} unless stated otherwise; EPR spectra were acquired from 0.22 μm-filtered aliquots at the indicated reaction times.

spins g^{-1} at 5 min to 0.7155×10^{15} spins g^{-1} at 30 min (Fig. S7), supporting the time-dependent accumulation of hydrogen-associated paramagnetic intermediates during aqueous corrosion. Although secondary contributions associated with interfacial gas–liquid perturbations cannot be fully excluded, the selective appearance of EPR features under aqueous corrosion conditions, and the dominant H_2 evolution signature in the CV response together support a coherent picture in which H_2 is the principal corrosion product, while transient H* forms concurrently at the same reactive sites. Collectively, these electrochemical and spin-spectroscopic results link the observed nanoscopic gas domains to a sustained, site-localized hydrogen-generation chemistry at the iron/water interface.

Conclusions

We demonstrated that HNBs are intrinsic products of the anaerobic aqueous corrosion of nZVI. Direct evidence was obtained from optical scattering and NTA, which identified dispersible nanoscale entities that are strongly suppressed by degassing, and from STXM, L-SEM, and AFM, which revealed low-density gas-related domains at or near the iron/water interface. CV and EPR further supported the association of these interfacial features with hydrogen-evolving corrosion chemistry and hydrogen-associated intermediates under aqueous conditions. Together, these results support a mechanism in which localized H_2 generation creates near-surface supersaturation and promotes heterogeneous nucleation within confined interfacial microenvironments. This work therefore extends iron corrosion from a purely solid–liquid description to a coupled gas–liquid–solid interfacial framework. More importantly, these transient interfacial gas domains may reshape local mass transfer, surface accessibility, and hydrogen-associated redox microenvironments, thereby influencing the reductive performance of nZVI in remediation systems.

Author contributions

Shuangjia Shi: writing – original draft, formal analysis, data curation, conceptualization. Qing Huang: methodology, data curation, investigation. Wei-xian Zhang: resources, supervision. Lijuan Zhang: resources, supervision, conceptualization. Airong Liu: writing – review & editing, project administration, investigation, funding acquisition, conceptualization.

Conflicts of interest

The authors declare that they have no known competing financial interests or personal relationships that could have appeared to influence the work reported in this paper.

Data availability

All data supporting the findings of this study are included within the manuscript and the accompanying supplementary information (SI).

Supplementary information: there are 16 pages in SI, including 3 tables and 6 figures. Text S1 and S2 provide chemical specifications and nZVI synthesis procedures; Text S3–S6 describe the STXM, AFM, L-SEM and NTA workflows; Text S7 and S8 give full protocols for cyclic voltammetry and EPR measurements. Fig. S1–S3 present the analytical workflow for HNB identification, including the NTA protocol, schematics of in-liquid STXM and *in situ* AFM imaging. Fig. S4–S7 provide the supporting control and quantitative data, including dissolved oxygen depletion during N_2 purging, filtration validation of particle removal, NTA quantification of HNBs formed during aqueous nZVI corrosion, and time-dependent EPR spin concentration analysis.

Movie of dynamic tracking of HNBs during aqueous nZVI corrosion (Video S1). See DOI: https://doi.org/10.1039/d6en00180g.

Acknowledgements

We thank the Beamline 08U1A at the SSRF for the sample preparation and STXM measurements. This work was supported by the National Natural Science Foundation of China (No. 12274427, 42073082, 12005284), and the National Key Research and Development Program of China (2022YFC3702102).

References

1 T. Lyu, S. Wu, R. J. G. Mortimer and G. Pan, Nanobubble Technology in Environmental Engineering: Revolutionization Potential and Challenges, *Environ. Sci. Technol.*, 2019, **53**, 7175–7176.
2 K. Ohgaki, N. Q. Khanh, Y. Joden, A. Tsuji and T. Nakagawa, Physicochemical approach to nanobubble solutions, *Chem. Eng. Sci.*, 2010, **65**, 1296–1300.
3 A. Agarwal, W. J. Ng and Y. Liu, Principle and applications of microbubble and nanobubble technology for water treatment, *Chemosphere*, 2011, **84**, 1175–1180.
4 X. Yang, L. Chen, S. Oshita, W. Fan and S. Liu, Mechanism for Enhancing the Ozonation Process of Micro- And Nanobubbles: Bubble Behavior and Interface Reaction, *ACS ES&T Water*, 2023, **3**, 3835–3847.
5 L. Tang, S. Zhou, F. Li, L. Sun and H. Lu, Ozone Micronanobubble-Enhanced Selective Degradation of Oxytetracycline from Production Wastewater: The Overlooked Singlet Oxygen Oxidation, *Environ. Sci. Technol.*, 2023, **57**, 18550–18562.
6 M. Jia, M. U. Farid, Y.-W. Ho, X. Ma, P. W. Wong, T. Nah, Y. He, M. W. Boey, G. Lu, J. K.-H. Fang, J. Fan and A. K. An, Advanced nanobubble flotation for enhanced removal of sub-10 μm microplastics from wastewater, *Nat. Commun.*, 2024, **15**, 9079.
7 K. Mensah, A. Magdaleno, S. Yaparatne, S. Garcia-Segura and O. G. Apul, Emerging investigator series: suspended air nanobubbles in water can shuttle polystyrene nanoplastics to the air–water interface, *Environ. Sci.: Nano*, 2024, **11**, 3721–3728.

8 Y. Luo, K. Fu, D. Wang and J. Luo, Nanobubble-Driven Interfacial Interactions of Carbon-Based Adsorbents with Legacy PFAS: Impact of Concentration, pH, and Coexisting Ions, *Environ. Sci. Technol.*, 2025, **59**, 6900–6914.
9 X. Jiang, W. Wang, G. Yu and S. Deng, Contribution of Nanobubbles for PFAS Adsorption on Graphene and OH- and NH2-Functionalized Graphene: Comparing Simulations with Experimental Results, *Environ. Sci. Technol.*, 2021, **55**, 13254–13263.
10 A. Bussonnière, Q. Liu and P. A. Tsai, Cavitation Nuclei Regeneration in a Water-Particle Suspension, *Phys. Rev. Lett.*, 2020, **124**, 034501.
11 M. R. Ghaani, P. G. Kusalik and N. J. English, Massive generation of metastable bulk nanobubbles in water by external electric fields, *Sci. Adv.*, 2020, **6**, eaaz0094.
12 S. Aluthgun Hewage, J. H. Batagoda and J. N. Meegoda, Remediation of contaminated sediments containing both organic and inorganic chemicals using ultrasound and ozone nanobubbles, *Environ. Pollut.*, 2021, **274**, 116538.
13 Y. Liu, T. Wu, J. C. White and D. Lin, A new strategy using nanoscale zero-valent iron to simultaneously promote remediation and safe crop production in contaminated soil, *Nat. Nanotechnol.*, 2021, **16**, 197–205.
14 A. M. Zafar, M. A. Javed, A. A. Hassan and M. M. Mohamed, Groundwater remediation using zero-valent iron nanoparticles (nZVI), *Groundw. Sustain. Dev.*, 2021, **15**, 100694.
15 Q. Huang, T. Gu, A. Liu, J. Liu and W.-x. Zhang, Probing pollutant reactions at the iron surface: a case study on selenite reactions with nanoscale zero-valent iron, *Environ. Sci.: Nano*, 2021, **8**, 2650–2659.
16 E. J. Reardon, Anaerobic Corrosion of Granular Iron: Measurement and Interpretation of Hydrogen Evolution Rates, *Environ. Sci. Technol.*, 1995, **29**, 2936–2945.
17 Y. Liu and G. V. Lowry, Effect of Particle Age (Fe0 Content) and Solution pH On NZVI Reactivity: H2 Evolution and TCE Dechlorination, *Environ. Sci. Technol.*, 2006, **40**, 6085–6090.
18 M. Liao, S. Zhao, G. Zhan, J. Liang, Z. Li, F. Dong, Y. Pan, H. Li and L. Zhang, Silicate-Confined Hydrogen on Nanoscale Zerovalent Iron for Efficient Defluorination Reactions, *J. Am. Chem. Soc.*, 2025, **147**, 3402–3411.
19 S. Maheshwari, C. van Kruijsdijk, S. Sanyal and A. D. Harvey, Nucleation and Growth of a Nanobubble on Rough Surfaces, *Langmuir*, 2020, **36**, 4108–4115.
20 H. Yang, H. Jiang, Y. Cheng, Y. Xing, Y. Cao and X. Gui, Solid-liquid interfacial nanobubble nucleation dynamics influenced by surface hydrophobicity and gas oversaturation, *J. Mol. Liq.*, 2024, **411**, 125758.
21 H. J. Qin, X. H. Guan, J. Z. Bandstra, R. L. Johnson and P. G. Tratnyek, Modeling the Kinetics of Hydrogen Formation by Zerovalent Iron: Effects of Sulfidation on Micro- and Nano-Scale Particles, *Environ. Sci. Technol.*, 2018, **52**, 13887–13896.
22 Y.-X. Huang, J. Guo, C. Zhang and Z. Hu, Hydrogen production from the dissolution of nano zero valent iron and its effect on anaerobic digestion, *Water Res.*, 2016, **88**, 475–480.
23 Y. Zhang, W. Fan, X. Li, W.-X. Wang and S. Liu, Enhanced Removal of Free Radicals by Aqueous Hydrogen Nanobubbles and Their Role in Oxidative Stress, *Environ. Sci. Technol.*, 2022, **56**, 15096–15107.
24 L. Xiao and N. Miwa, Hydrogen Nano-Bubble Water Suppresses ROS Generation, Adipogenesis, and Interleukin-6 Secretion in Hydrogen-Peroxide- or PMA-Stimulated Adipocytes and Three-Dimensional Subcutaneous Adipose Equivalents, *Cells*, 2021, **10**, 626.
25 W. K. Kim, G. Hong, Y. H. Kim, J. M. Kim, J. Kim, J. G. Han and J. Y. Lee, Mechanical Strength and Hydration Characteristics of Cement Mixture with Highly Concentrated Hydrogen Nanobubble Water, *Materials*, 2021, **14**, 2735.
26 W. Fan, Y. Zhang, S. Liu, X. Li and J. Li, Alleviation of copper toxicity in Daphnia magna by hydrogen nanobubble water, *J. Hazard. Mater.*, 2020, **389**, 122155.
27 S. Liu, J. Li, S. Oshita, M. Kamruzzaman, M. Cui and W. Fan, Formation of a Hydrogen Radical in Hydrogen Nanobubble Water and Its Effect on Copper Toxicity in *Chlorella*, *ACS Sustainable Chem. Eng.*, 2021, **9**, 11100–11109.
28 A. Liu, J. Liu, J. Han and W.-X. Zhang, Evolution of nanoscale zero-valent iron (nZVI) in water: Microscopic and spectroscopic evidence on the formation of nano- and micro-structured iron oxides, *J. Hazard. Mater.*, 2017, **322**, 129–135.
29 X.-q. Li and W.-x. Zhang, Iron Nanoparticles: the Core−Shell Structure and Unique Properties for Ni(II) Sequestration, *Langmuir*, 2006, **22**, 4638–4642.
30 Q. Huang, J. Qi, L. Zhou, Y. Wang, W. X. Zhang, J. Hu, R. Tai, S. Wang, A. Liu and L. Zhang, Hydrogen Nanobubbles Generated In Situ from Nanoscale Zerovalent Iron with Water to Further Enhance Selenite Sequestration, *Environ. Sci. Technol.*, 2024, **58**, 4357–4367.
31 Y. Tian, Z. Qiu, R. Dai and Z. Wang, Tailoring morphology and performance of polyamide nanofiltration membrane via nanobubble dissolution regulation, *Chin. Chem. Lett.*, 2026, **37**, 111251.
32 L. Zhang, C. Wang, R. Tai, J. Hu and H. Fang, The Morphology and Stability of Nanoscopic Gas States at Water/Solid Interfaces, *ChemPhysChem*, 2012, **13**, 2188–2195.
33 Y. Chai, F. Wang, Y. Gao, P. Wang, Z.-y. Jia, X.-J. Li, Y. Dong and C.-C. Wang, Ozone activation over core-shell nanoreactors for enhanced organic pollutants degradation: Surface-bound superoxide radicals induced by confinement effect, *Environ. Res.*, 2025, **282**, 122099.
34 T. Liu, S. Xiao, N. Li, J. Chen, X. Zhou, Y. Qian, C.-H. Huang and Y. Zhang, Water decontamination via nonradical process by nanoconfined Fenton-like catalysts, *Nat. Commun.*, 2023, **14**, 2881.
35 Q. Huang, S. Shi, C. Chen, W.-x. Zhang, J. Hu, J. Li, L. Zhang and A. Liu, Hydrogen Nanobubbles Promote As(III) Transformation on the Nanoscale Zero-Valent Iron Interface in an Aquatic System, *ACS Appl. Mater. Interfaces*, 2026, 21255–21264.
36 Z.-C. Zhang, R.-X. Mei, F.-X. Wang, J.-F. Wang, Y.-L. Dong and C.-C. Wang, MOF-on-MOF derived magnetic CoFe2O4@Fe0 nanocomposites for ultra-rapid peroxymonosulfate activation:

mechanistic insights and eco-toxicological validation, *Environ. Sci.: Nano*, 2025, **12**, 4843–4849.
37 G. R. Buettner, Spin Trapping: ESR parameters of spin adducts 1474 1528V, *Free Radical Biol. Med.*, 1987, **3**, 259–303.
38 A. J. Carmichael, K. Makino and P. Riesz, Quantitative Aspects of ESR and Spin Trapping of Hydroxyl Radicals and Hydrogen Atoms in Gamma-Irradiated Aqueous Solutions, *Radiat. Res.*, 1984, **100**, 222–234.